Nano Research

Open Access

Research Article

Semimetallic Nb/Ta-Te phases with charge density wave for mid- and long-wave infrared detection

Hao Gu[1,2,§], Suifeng Xiong[1,2,§], Zhongyang Yu[2], Futing Sun[1,4], Chao Guo[1], Jingyu Zhang[1], Wen Chen[1], Yunluo Wang[1], Zesen Gao[1], Haoxuan Li[2], Xinyue Zhao[1], Xiaohan Zhang[1], Qirui Sun[2], Lili Yang[1], Yongzhe Wang[4], He Zhu[2] ✉, Yufeng Shan[2,3] ✉, Haijie Chen[1] ✉, and Ning Dai[2,3,5]

[1] *State Key Laboratory of Advanced Fiber Materials, Materials College of Materials Science and Engineering, Donghua University, Shanghai 201620, China*
[2] *Infrared material fellowship (IMF), Hangzhou Institute for Advanced Study, University of Chinese Academy of Sciences, Hangzhou 310024, China*
[3] *State Key Laboratory of Infrared Physics, Shanghai Institute of Technical Physics, Chinese Academy of Sciences, Shanghai 200083, China*
[4] *State Key Laboratory of High Performance Ceramics, Shanghai Institute of Ceramics, Chinese Academy of Sciences, Shanghai 200050, China*
[5] *Jiangsu Collaborative Innovation Center of Photovoltaic Science and Engineering, Changzhou 213164, China*
[§] *Gu Hao and Suifeng Xiong contributed equally to this work.*

Cite this article: *Nano Research*, **2026**, *19*, 94908526. https://doi.org/10.26599/NR.2026.94908526

ABSTRACT: Charge density wave (CDW), which typically opens a narrow energy gap near the Fermi level, is highly sensitive to low-energy photon excitations, providing a compelling basis for infrared detectors. Here, we systematically investigated one-dimensional (1D) $NbTe_4$ and $TaTe_4$, as well as two-dimensional (2D) $NbTe_2$ and $TaTe_2$, from the binary Nb/Ta-Te systems for mid- and long-wave infrared detection. They all exhibit notable infrared photoresponse under zero-bias (self-powered) operation governed by the photothermoelectric effect. $NbTe_2$, in particular, achieves detectivities of 1.64×10^8 and 1.29×10^8 Jones under illumination of 4 and 8.47 μm infrared lights, respectively. Using artificial intelligence, super-resolution reconstruction was realized to enhance images obtained from photodetector-based single-pixel imaging, laying an important foundation for computing-in-memory integration. This work highlights Nb/Ta-Te phases as promising candidates for infrared detectors, paving the way for next-generation room-temperature, low-power intelligent infrared optoelectronic systems.

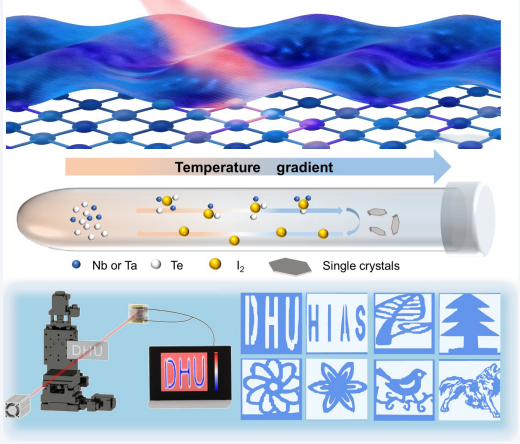

KEYWORDS: charge density wave (CDW), broadband photodetectors, Nb/Ta-Te binary systems, artificial intelligence

1 Introduction

Charge density wave (CDW), as a symmetry-breaking ordered state, manifests as a periodic spatial modulation of the conduction electrons that is coupled with periodic lattice distortion [1–7]. CDW is closely related to some emergent phenomena in condensed materials, such as unconventional superconductivity, mott insulator, etc. [8, 9]. The weak CDW state is sensitive to external perturbations—including electrical field, gating voltages, and optical excitation—offering intriguing opportunities for electronic and optoelectronic applications [3]. The periodic modulation induced by lattice distortion establishes a potential landscape that folds the Brillouin zone, couples electronic states near the Fermi surface, and thereby opens a band gap or pseudo-gap, endowing the material with specific responsiveness to low-energy photons such as infrared light [10, 11]. Moreover, the fluctuation of CDW exhibits collective excitations [12], in which electrons no longer behave as independent entities but instead form a coherent quantum condensate [13, 14]. Under photon irradiation, this collective coherence and quantum transport can facilitate the motion of additional charge carriers, leading to giant photocurrent gain, and enabling detectors to sense weak optical signals [12, 15].

Received: November 7, 2025; **Revised:** January 13, 2026
Accepted: February 3, 2026

✉Address correspondence to He Zhu, anthonyzhu1990@hotmail.com; Yufeng Shan, shanyufeng@mail.sitp.ac.cn; Haijie Chen, haijie.chen@dhu.edu.cn

CDW materials offer unique potential for realizing high-performance, broadband photodetectors. To date, there have been some reports on photodetectors based on CDW materials. For instance, $(TaSe_4)_2I$ photodetectors exhibit a high responsivity of 1.18×10^3 A/W in the mid-infrared region under a bias of 3 V [13]. Devices fabricated from 2H-VSe_2 achieve a responsivity of 75.26 A/W with detectivity exceeding 10^{10} Jones in the visible to near-infrared range under 1 V bias [16]. Rare-earth tritelluride based broadband photodetectors operating in self-powered mode exhibit spectral response from ultraviolet to mid-wave infrared, showing a detectivity of 1.26×10^9 Jones at 3500 nm, comparable to graphene-based photodetectors dominated by photothermoelectric (PTE) effects [10]. These CDW-based photodetectors not only demonstrate superior optoelectronic performance but also show exceptional sensitivity across the communication band as well as the mid- and long-wave infrared regions. Among the diverse CDW materials, the binary Nb/Ta-Te family stands out due to its unique low-dimensional structures and robust CDW properties, offering a potential platform for broadband photodetection. This family, comprising 1D $NbTe_4$ and $TaTe_4$ as well as 2D $NbTe_2$ and $TaTe_2$, represents a class of materials exhibiting pronounced CDW behaviors [17–21]. Both $NbTe_4$ and $TaTe_4$ crystallize in the *P4/mcc* space group, where each Nb or Ta atom is coordinated with eight Te atoms, forming face-shared square antiprismatic chains along the *c*-axis [18, 22]. This bonding configuration leaves sufficient free charge in the d-band of Nb or Ta atoms for electrical conduction, while the low-dimensional nature of the structure provides a favorable environment for CDW transitions [23]. The CDW transition temperatures of $NbTe_4$ and $TaTe_4$ are 520 and 475 K, respectively [22–24]. In contrast, $NbTe_2$ and $TaTe_2$ adopt monoclinic structures with the *C2/m* space group [17, 25]. Their CDW transition temperatures are about 550 K for $NbTe_2$ and 400 K for $TaTe_2$, respectively [26, 27]. The intriguing interplay between low dimensionality and strong CDW order in this material family renders them highly promising for optoelectronic applications. However, systematic investigations into their broadband photodetection remain scarce, with only a few studies reporting photoresponse of $NbTe_4$ and $TaTe_2$ in the near-infrared range (355 to 2715 nm), showcasing their latent potential [28, 29].

In this work, we systematically investigated the photodetection performance of 1D $NbTe_4$, $TaTe_4$, and 2D $NbTe_2$, $TaTe_2$ for the mid-to-long-wave infrared detection. High-quality single crystals were successfully synthesized via chemical vapor transport, and their structures were characterized in detail. Optoelectronic measurements show that all materials exhibit a significant mid- to long-wavelength infrared response dominated by the PTE effect in the self-powered (zero bias) mode. For $NbTe_2$, its responsivity and detectivity at 4 μm wavelength reached 2.76 mA/W and 1.64×10^8 Jones, respectively. We have constructed a single-pixel imaging system centered on a self-powered Nb/Ta-Te detector. Using this system, we successfully reconstructed a series of target images and applied a U-Net-based deep learning network for image super-resolution reconstruction. The model effectively enhanced the clarity of images obtained through single-pixel imaging, achieving a high accuracy of 96.4% and a low loss value of 0.035. This technology preliminarily establishes a complete technical chain spanning from materials and devices to system applications, providing a feasible material platform and solution for the development of a new generation of room-temperature, low-power, intelligent infrared optoelectronic systems.

2 Results and discussion

2.1 Synthesis and characterizations of Nb/Ta-Te CDW materials

Since its proposal, the theory of CDW has inspired extensive research and is now recognized as a universal electronic collective phenomenon in condensed matter physics [30]. For 1D materials, the CDW phase transition can be explained by Peierls theory. When each atom contributes one electron, the resulting half-filled energy band leads to metallic behavior. However, upon considering electron–phonon interactions, the 1D atomic chain becomes unstable at low temperatures, causing a periodic lattice distortion. During this distortion, adjacent atoms move closer together, doubling the lattice periodicity and opening a bandgap at π/(2a)—the new Brillouin zone boundary—thereby driving the system from a metallic to an insulating state [30–32]. The origin of CDWs in two-dimensional (2D) materials is more complex and remains under debate. While Fermi surface nesting and saddle-point mechanisms can account for certain systems [33–36], studies of prototypical materials such as 2H-$NbSe_2$ suggest that wavevector-dependent strong electron–phonon coupling is likely the dominant driving force [37, 38]. In contrast, other transition-metal dichalcogenides, such as 1T-$TiSe_2$, may involve multifaceted mechanisms including the Jahn–Teller effect or excitonic-insulator formation [39, 40]. Figure 1(a) schematically illustrates the collective excitation characteristics of CDWs. Under illumination, the coherent quantum condensate formed in CDW materials can channel additional electrons through the circuit, resulting in a giant photocurrent gain.

Figures S1(a) and S1(b) in the Electonic Supplementary Material (ESM) present the phase diagrams for the Nb-Te and Ta-Te systems, respectively. The Nb-Te system includes stable phases such as Nb_5Te_4, Nb_3Te_4, $NbTe_2$, and $NbTe_4$, whereas the Ta-Te system contains the stable phases of $TaTe_2$ and $TaTe_4$. In our investigation into the photodetection properties of $NbTe_2$, $NbTe_4$, $TaTe_2$, and $TaTe_4$, we synthesized these four single crystals using chemical vapor transport. Figure 1(b) schematically depicts the CVT growth process. I_2 serves as the transport agent, while Nb or Ta and Te powders act as raw materials. The powder X-ray diffraction (PXRD) patterns (Fig. 1(d)) demonstrate that the primary peaks closely match the standard diffraction patterns for $NbTe_2$ (PDF #21-0605), Nb_3Te_4 (PDF #72-1122), $TaTe_2$ (PDF #21-1201), $NbTe_4$ (PDF #18-0926), and $TaTe_4$ (PDF #18-1314) crystals. All diffraction peaks perfectly match their respective standard patterns with sharp peak shapes and no impurity peaks, confirming the successful acquisition of highly phase-pure single-crystal samples. Figure 1(e) presents an optical photograph of a typical single crystal, revealing plate-like or rod-shaped crystals with dimensions reaching hundreds of micrometers and smooth surfaces, laying the foundation for subsequent micro-nano device fabrication.

Figure 1(c) presents the crystal structure models of these four compounds. $NbTe_2$ and $TaTe_2$ exhibit typical layered two-dimensional structures, while $NbTe_4$ and $TaTe_4$ feature 1D chain-like structures. $NbTe_2$ is a transition metal dichalcogenide belonging to the *C2/m* space group, where Nb atoms are sandwiched between Te atoms. $TaTe_2$ exhibits a similar structure. $NbTe_4$ crystallizes in a tetragonal structure within the *P4/mcc* space group, with each niobium atom coordinated by eight Te atoms, forming 1D chains along the *c*-axis. The structure of $TaTe_4$ is analogous to that of

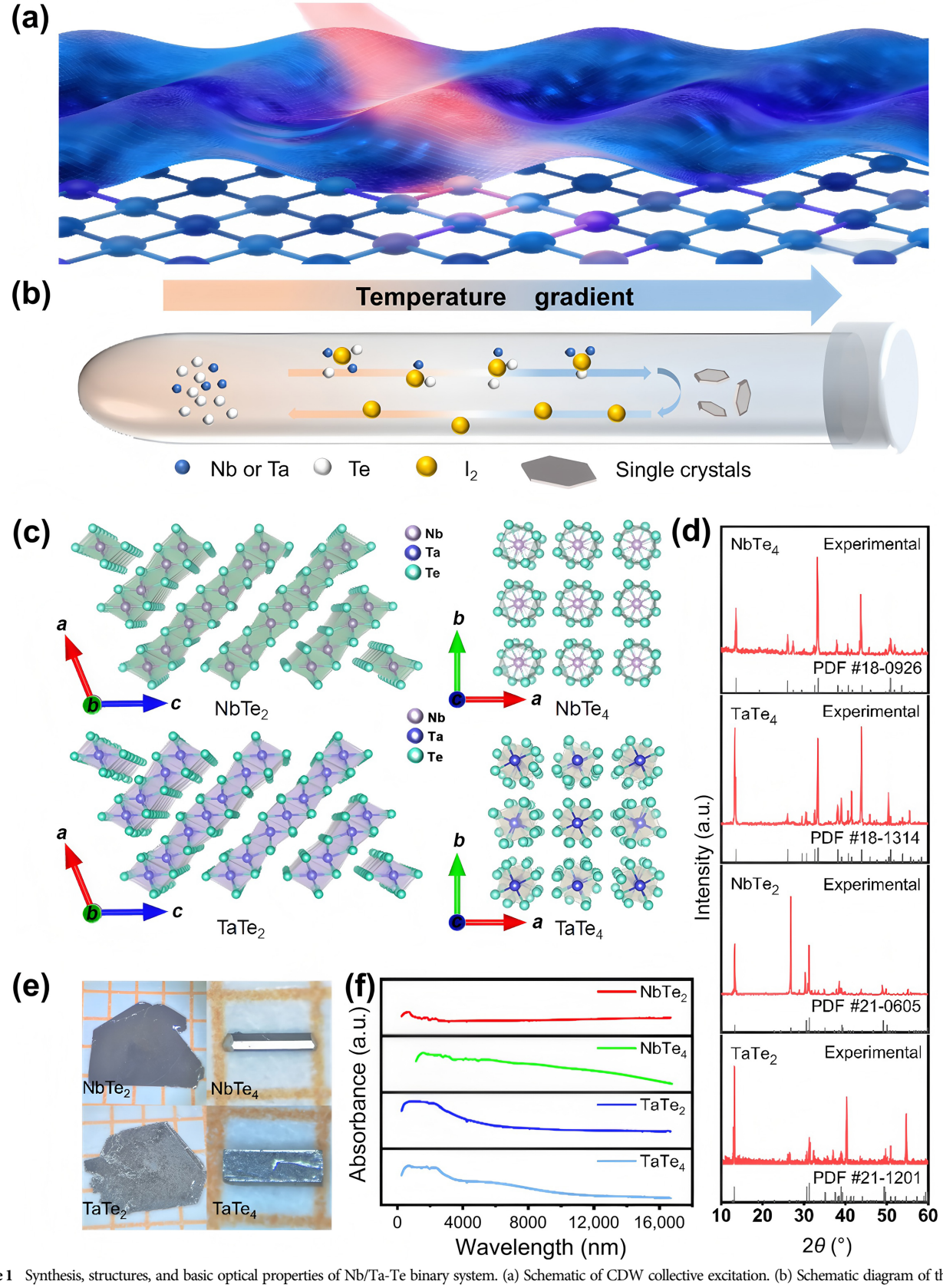

Figure 1 Synthesis, structures, and basic optical properties of Nb/Ta-Te binary system. (a) Schematic of CDW collective excitation. (b) Schematic diagram of the CVT method used to synthesize Nb/Ta-Te single crystals. (c) Schematic crystal structures of $NbTe_2$, $TaTe_2$, $NbTe_4$, and $TaTe_4$ demonstrating 2D layered and 1D chain structures, respectively. (d) Comparison of the PXRD pattern of the as-synthesized Nb/Ta-Te single crystals with the standard pattern. (e) Optical photograph of the synthesized $NbTe_2$ crystals. The image was taken on standard graph paper, where the side length of each grid square corresponds to 1 mm. (f) Broad-spectrum absorption spectra of the four compounds from the UV to the far IR.

$NbTe_4$. To verify the composition of the single crystals, we employed scanning electron microscopy (SEM) combined with energy-dispersive X-ray spectroscopy (EDS) for elemental mapping. The SEM images clearly reveal the crystal morphology, while EDS elemental maps demonstrate uniform distribution of Nb and Te in a 1:2 ratio (Fig. S2 in the ESM), confirming the chemical composition. Similarly, elements in $NbTe_4$, $TaTe_2$, and $TaTe_4$ are uniformly distributed throughout the synthesized samples.

To provide direct structural evidence of the charge density wave (CDW) state, single crystal X-ray diffraction (SCXRD) was performed. As shown in the reciprocal space reconstruction of the (011) plane for $TaTe_4$ (Fig. S3 in the ESM), distinct satellite reflections are observed surrounding the fundamental Bragg peaks. These satellite spots originate from the periodic lattice distortion associated with the CDW superlattice modulation, confirming the existence of the distorted structural phase at room temperature. To explicitly verify the CDW phase transition, we performed temperature-dependent resistance measurements. As shown in Fig. S4 in the ESM, the resistivity exhibits a typical metallic behavior in the low-temperature regime. Upon heating, a pronounced resistivity anomaly appears at T_{CDW} ~ 550 K. This characteristic transition temperature is in excellent agreement with previous reports for the monoclinic-to-rhombohedral structural phase transition in $NbTe_2$ driven by CDW formation. The observation of such a sharp transition feature serves as robust evidence for the high phase purity of our synthesized crystals. Complementing the transport data, Fig. S5 in the ESM displays the room-temperature Raman spectrum of the $NbTe_2$ sample.

To accurately identify the vibrational modes, the raw spectrum was deconvoluted using Lorentzian peak fitting. The analysis resolves three dominant peaks centered at 84, 117, and 137 cm^{-1}, along with a broad feature around 218 cm^{-1}. The detection of the low-frequency mode at 84 cm^{-1} is critical for phase identification. This feature corresponds to the A_g^3 lattice breathing mode of the distorted monoclinic phase $C2/m$, in excellent agreement with the theoretical frequency of 86 cm^{-1} predicted by DFT calculations. In the high-temperature undistorted 1-T phase $P\bar{3}m1$, Raman activity in this low-frequency region is symmetry-forbidden. Therefore, the emergence of the 84 cm^{-1} mode serves as a spectral fingerprint for the phonon zone folding effect, confirming the formation of the CDW superlattice. The peaks at 117 and 137 cm^{-1} are assigned to the A_g^4 and A_g^5 modes, respectively, with their positions consistent with the phonon characteristics of few-layer $NbTe_2$ [41, 42].

We systematically investigated the surface chemical composition and valence state evolution of $NbTe_2$ single crystals before and after Ar^+-ion sputtering using X-ray photoelectron spectroscopy (XPS). The results reveal that the Nb 3d spectra of pristine samples exhibit characteristic signals of Nb^{4+} along with a minor Nb^{5+} component, which originates from a superficial oxidation layer (Fig. S6(a) in the ESM). Following Ar^+-ion sputtering treatment, the Nb^{5+} signature shows significant attenuation in the Nb 3d spectra, while the Nb^{4+} state becomes predominant, demonstrating effective removal of surface oxides and exposure of the intrinsic $NbTe_2$ crystalline structure (Fig. S6(d) in the ESM). It is worth noting that the Te 3d spectrum maintains a consistent peak shape throughout the process, and no new valence states are detected before and after sputtering and no Te vacancies are observed (Figs. S6(c) and S6(f) in the ESM).

To evaluate the photodetection potential of these materials, we measured their absorption spectra from the ultraviolet to the far-infrared region, with results shown in Fig. 1(f). Most notably, all four compounds exhibit strong, flat, broadband absorption spanning from the UV–visible region to the mid-to-long-wave infrared band up to approximately 16 μm. This broadband light absorption behavior originates from the intrinsic zero bandgap electronic structure of the semimetal, where the conduction and valence bands cross at the Fermi level, endowing $NbTe_2$ with superior light absorption capabilities across a broad wavelength range. Particularly, its strong absorption in the 8–14 μm atmospheric window band (critical for detecting human thermal radiation) directly demonstrates that the Nb/Ta-Te series CDW materials selected in this work are highly promising candidates for room-temperature, broadband, and especially mid-to-long-wave infrared photodetection.

To assess the thermal stability of the synthesized crystals, differential scanning calorimetry (DSC) measurements were performed over a wide temperature range. As shown in Fig. S7 in the ESM, the DSC curves for $NbTe_2$, $TaTe_2$, $NbTe_4$, and $TaTe_4$ remain smooth with a flat baseline across the low-to-medium temperature region (200–600 °C). Distinct endothermic or exothermic peaks are only observed at elevated temperatures exceeding 600–700 °C, corresponding to the melting or decomposition of the crystals. The absence of thermal anomalies below 600 °C demonstrates the excellent thermal stability of these materials, ensuring their durability under PTE device operation conditions where local heating occurs.

2.2 Spatially resolved photocurrent response of 1D $NbTe_4$ and $TaTe_4$

To investigate the infrared photoresponse properties of 1D $NbTe_4$ and $TaTe_4$ crystals in depth, we fabricated dual-electrode devices with a metal-semiconductor-metal (MSM) structure (Fig. 2(a)) and systematically studied their spatially resolved photocurrent response under zero bias. All measurements were conducted using mid-to-long-wave infrared lasers at 4 and 8.47 μm, directly verifying the materials' detection capability in this wavelength range.

We analyzed the potential photoelectric response mechanisms of the photodetector. Typically, the photoresponse of a photodetector can arise from one or more effects, including photoconductivity (PC), bolometric (BOL), photovoltaic (PV), or PTE effects. Among these, the PC and BOL effects generally require an external bias voltage to generate photocurrent, while devices relying on PV and PTE effects can operate without a bias voltage. Firstly, we visually revealed the spatial distribution characteristics of the photoresponse through scanning photocurrent imaging. Figure 2(b) displays the photocurrent mapping of the $TaTe_4$ device under infrared illumination. It is clearly observable that the magnitude and polarity (positive/negative) of the photocurrent signal strongly depend on the precise position of the laser spot on the channel. Specifically, a positive current is measured when the spot is near one electrode, while the current becomes negative when the spot scans near the other electrode. This typical spatially symmetric distribution is a hallmark of the PTE effect.

To quantitatively analyze this phenomenon, point-scanning measurements were performed along the channel axis. Figure 2(c) plots the position-dependent photocurrent measured for $NbTe_4$ and $TaTe_4$. Both exhibits highly consistent trends: photocurrent values transition from a negative maximum at one electrode end to a positive maximum at the opposite end, approaching zero at the channel midpoint. This curve demonstrates the theoretically

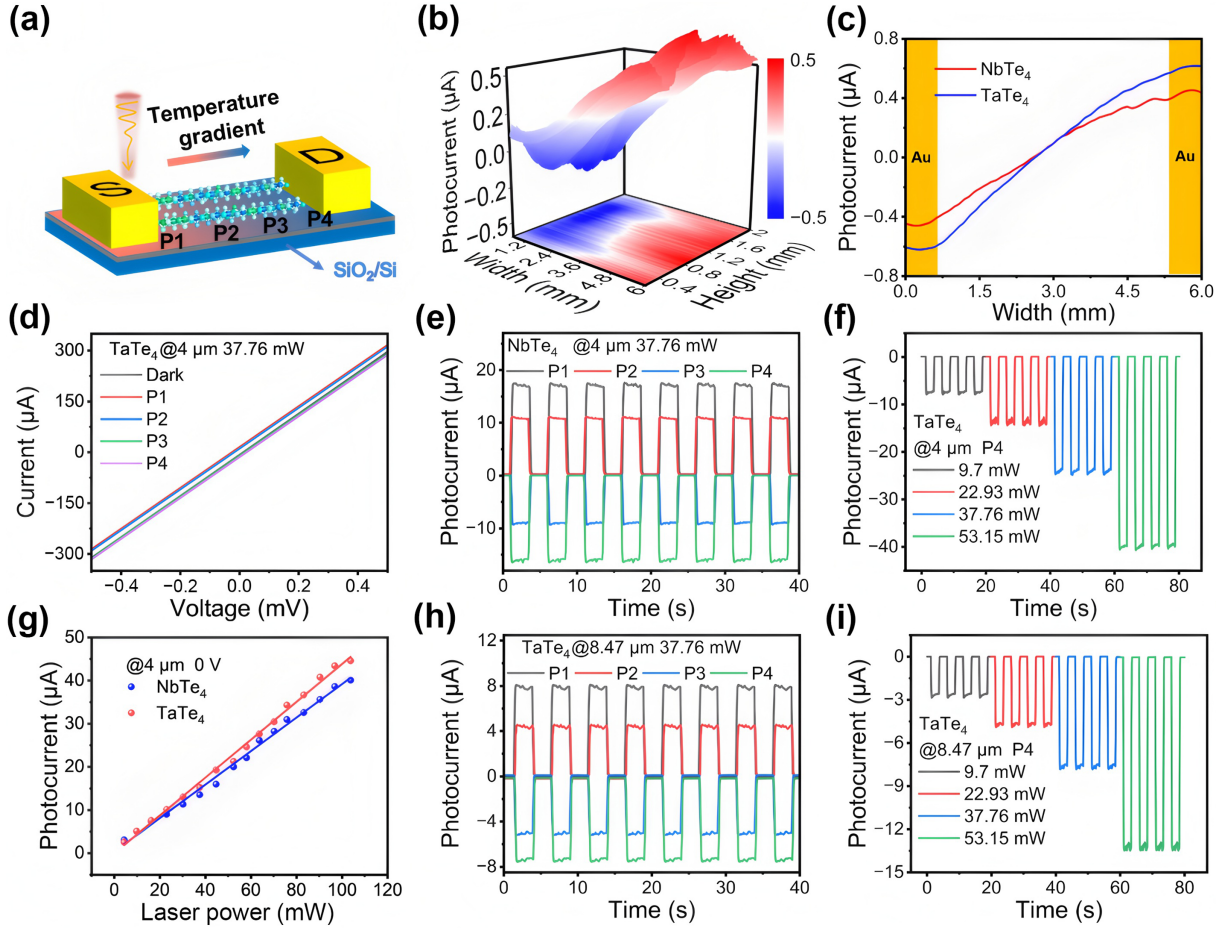

Figure 2 Spatially resolved photocurrent properties of 1D $NbTe_4$ and $TaTe_4$ crystals. (a) Schematic diagram of the device structure of the one-dimensional material. (b) Photocurrent mapping of the $TaTe_4$ device. (c) Steady-state photocurrent versus position curves for $NbTe_4$ and $TaTe_4$. (d) Current–voltage curves of the $TaTe_4$ devices at different light positions (P1–P4) under a 4 μm laser. (e) Current–time response curves of $NbTe_4$ at points P1–P4. (f) Current–time curves at different powers for the P4 position of the $TaTe_4$ device under 4 μm laser irradiation. (g) Linear dependence of photocurrent on laser power at 4 μm. (h) Current–time response curves of $TaTe_4$ at points P1–P4. (i) Current–time curve of $TaTe_4$ at 8.47 μm with fixed position of P4 and varying power

predicted linear positional variation of photocurrent for the PTE effect. Specifically, a photothermal voltage ($P_{VTE} = -S\Delta T$) arises from the temperature gradient (ΔT) between the laser spot and the electrodes at either end, driven by the material's Seebeck coefficient (Fig. S8 in the ESM). This voltage induces current flow within the circuit.

To further confirm device contact quality and validate the PTE effect mechanism, we measured current–voltage (I–V) curves at four positions (P1–P4) under 4 μm laser irradiation with fixed laser power (Fig. 2(d), and Figs. S10(a), S10(b), and S10(c) in the ESM). All curves exhibited linear behavior and were mutually parallel. This result first confirms the formation of excellent ohmic contacts between the metal electrodes and the Nb/Ta-Te crystals, ruling out the possibility of Schottky junctions dominating the optical response. More importantly, the parallel I–V curves indicate that the device's internal resistance remains constant under illumination at different positions. Notably, devices based on the photovoltaic effect are often influenced by complex factors within the internal junction region, leading to nonlinear output characteristic curves. However, our device exhibits a distinctly linear output, suggesting that its photoresponse is primarily driven by the PTE effect. The current exhibits change in both sign and magnitude, which provides further compelling evidence for the PTE effect.

The device's dynamic response characteristics were evaluated via current–time (I–t) curves. As shown in Figs. 2(e), 2(f), and 2(h), and Figs. S10(d) and S10(f) in the ESM, laser modulation was achieved using a signal generator to implement switching operations. The device exhibited rapid, stable, and reproducible optical switching characteristics at all points P1–P4. The polarity of the photocurrent also varied with position, fully consistent with the static measurements in Fig. 2(c), demonstrating reliable response speed and stability in self-powered mode.

Next, we examined the dependence of photocurrent on incident laser power. At a 4 μm wavelength, Fig. 2(g) shows that both $NbTe_4$ and $TaTe_4$ exhibit good linearity between photocurrent and laser power at zero bias. This linear dependence is a hallmark of PTE detectors, indicating stable photothermal conversion efficiency across the tested power range without saturation or damage—for quantitative light intensity detection in practical applications.

Finally, we further validated the universality of the aforementioned mechanism and device performance at longer infrared wavelengths (8.47 μm). Figure S10(e) in the ESM displays a family of I–V curves measured at position P4 of the $NbTe_4$ device as the laser power varies. A linear and parallel relationship is again observed, reaffirming the validity of the ohmic contact and PTE mechanism in the long-wave infrared band. Figure 2(i) records the

I–*t* curve of $TaTe_4$ at the P4 position under varying laser power at 8.47 μm. Figure S10(a) in the ESM shows the *I*–*t* curves of $TaTe_4$ at different positions under the same power. The light current amplitude increases monotonically with power, exhibiting an excellent signal-to-noise ratio. This fully demonstrates the material's highly efficient and stable photothermal energy conversion capability in the mid-to-long infrared region.

2.3 Spatially resolved photocurrent response of 2D $NbTe_2$ and $TaTe_2$

We further investigated the optoelectronic properties of 2D $NbTe_2$ and $TaTe_2$ crystals. As shown in the MSM device structure depicted in Fig. 3(a), we systematically evaluated their optical response characteristics in the mid-to-long infrared wavelength range under self-powered mode at zero bias. Figure 3(b) displays the spatially resolved photocurrent mapping of the $NbTe_2$ device under infrared illumination. Similar to 1D materials, the magnitude and polarity of the photocurrent signal strongly depend on the laser spot position, exhibiting a typical spatial distribution with positive response near one electrode and negative response near the other. This preliminary observation suggests a PTE effect as the response mechanism.

To quantitatively analyze this spatial dependency, similar to 1D materials, we performed point-scanning measurements along the channel axis. Figure 3(c) plots the steady-state photocurrent measured for both $NbTe_2$ and $TaTe_2$. Both materials exhibit a transition of photocurrent values from negative to positive with positional change, fully consistent with PTE effect theory predictions. Combined with the Seebeck coefficients measured in the supporting information (Fig. S8 in the ESM), this confirms that the response of 2D materials is also driven by laser-induced temperature gradients.

We further validated the device contact quality and intrinsic mechanism (Fig. 3 and Fig. S11 in the ESM). We performed identical characterizations. Under 4 μm laser irradiation at fixed power, Fig. 3(d) shows that all *I*–*V* curves of $NbTe_2$ devices measured at positions P1–P4 are linear and parallel to each other. This first demonstrates excellent ohmic contacts. Second, the parallel *I*–*V* curves indicate that illumination introduces only a position-dependent photothermal voltage while the device resistance remains constant, providing crucial evidence for the PTE effect.

The dynamic response of the devices was evaluated via *I*–*t* curves. Figure 3(e) shows the response of $NbTe_2$ at positions P1–P4 to modulated laser light, exhibiting fast, stable, and reproducible switching characteristics with the photoelectric current polarity changing regularly according to position. Figure 3(h) records the *I*–*t* curve of $TaTe_2$ under identical conditions, demonstrating excellent stability. The dependence of photocurrent on incident laser power is shown in Fig. 3(g). At the 4 μm wavelength, both

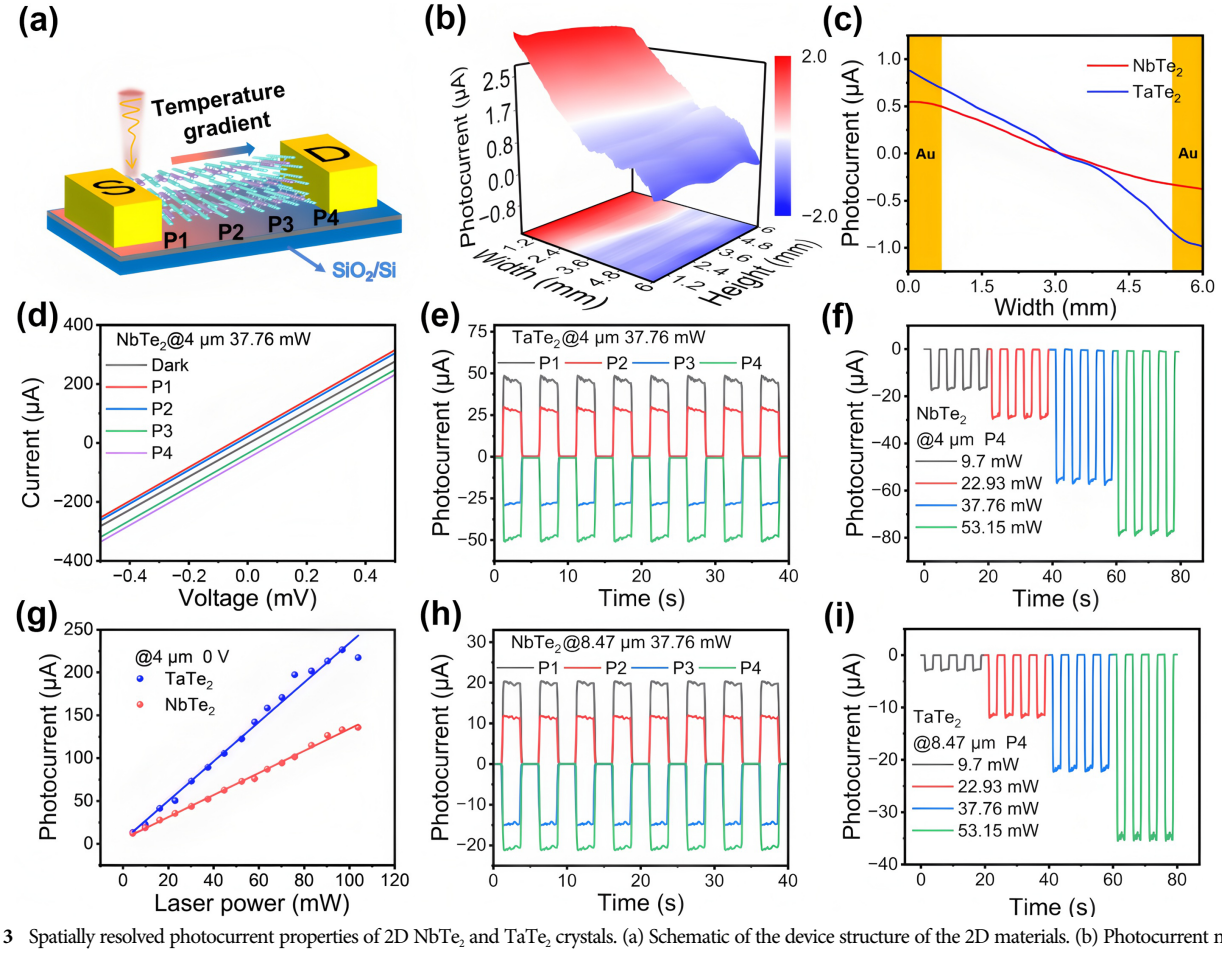

Figure 3 Spatially resolved photocurrent properties of 2D $NbTe_2$ and $TaTe_2$ crystals. (a) Schematic of the device structure of the 2D materials. (b) Photocurrent mapping of the $NbTe_2$ devices. (c) Steady-state photocurrent versus position curves for $NbTe_4$ and $TaTe_4$. (d) Current–voltage curves of $NbTe_2$ devices at different light positions (P1–P4) under a 4 μm laser. (e) Current–time response curves of $TaTe_2$ at points P1–P4. (f). Current–time curves at different powers for the P4 position of the $NbTe_2$ device under 4 μm laser irradiation. (g) Linear dependence of photocurrent on laser power at 4 μm. (h) Current–time response curves of $NbTe_2$ at points P1–P4. (i) Current–time curve of $TaTe_2$ at 8.47 μm with fixed position at P4 and varying power.

$NbTe_2$ and $TaTe_2$ exhibit good linearity between photocurrent and laser power at zero bias, indicating stable photothermal conversion efficiency across the tested power range and suitability for quantitative light intensity detection.

We similarly validated this behavior using an 8.47 μm laser. Figure S11(e) in the ESM displays the *I*–*V* curves of $TaTe_2$ at different positions (P1–P4), maintaining linear and parallel relationships. Figure 3(i) records the evolution of $TaTe_2$ photocurrent with increasing laser power at 8.47 μm when fixed at position P4. It clearly shows the photocurrent amplitude monotonically increasing with power, proving that 2D materials also possess high-efficiency photothermal-to-electric energy conversion capabilities in the long-wave infrared region. Furthermore, quantitative analysis of the time-resolved photoresponse at symmetric channel positions (P1 and P4) reveals that the photocurrent magnitude deviation is less than 5% (Fig. S12 in the ESM). This exceptional spatial uniformity across the macroscopic device channel serves as robust evidence for the high crystalline quality and phase homogeneity of the synthesized single crystals.

2.4 Optoelectronic performance of Nb/Ta-Te assembled devices

In summary, through systematic spatially resolved optoelectronic measurements of 1D ($NbTe_4$, $TaTe_4$) and 2D ($NbTe_2$, $TaTe_2$) Nb/Ta-Te series crystals, we confirm that the PTE effect dominates their mid-infrared response. This conclusion is supported by key evidence, including spatial polarity reversal, excellent ohmic contact, rapid dynamic response, and good power linearity. This research not only unifies our understanding of the photovoltaic behavior of this material series across different dimensions but also highlights its application potential. 1D materials hold great promise for developing novel self-powered broadband detectors, while 2D materials with layered structures lay the foundation for integrated optoelectronic devices. The responsivity (*R*) of a photodetector measures its ability to convert light signals into electrical signals. It is defined as Eq. (1)

$$R = \frac{I_{ph}}{PA} \tag{1}$$

where I_{ph} is the photocurrent, *P* is the light power density, and *A* is the effective area of the photodetector [43, 44]. Our device exhibits excellent responsivity across the mid to long wave infrared ranges, highlighting its potential for broadband photodetection applications. Furthermore, the specific detectivity (D^*) is crucial for assessing a photodetector's capacity to detect feeble signals. D^* is defined as Eq. (2) [43–45]

$$D^* = R\frac{\sqrt{A}}{S_n} \tag{2}$$

where *R* is the responsivity, and S_n represents the current noise density from the noise spectrum (Fig. 4(b) and Fig. S13 in the ESM).

Having confirmed the dominant PTE mechanism, we systematically evaluated key performance parameters of photodetectors based on Nb/Ta-Te series single crystals, including response time, detectivity, responsivity, and stability, to comprehensively assess their application potential in mid-to-long-wave infrared detection. Since the responses of all devices originate from the PTE effect, their speeds are mainly limited by the lattice thermal relaxation process, and thus the response times are on the order of tens of milliseconds [46]. Figure 4(a) illustrates a typical response time profile of the best-performing $NbTe_2$ device with rise and fall times of 69.9 and 70.1 ms, respectively, demonstrating good transient response repeatability. The response times of the other materials are slightly slower, but in line with what is expected from the PTE mechanism (Fig. S14 in the ESM). Although this response rate is not suitable for ultrafast detection applications, it is sufficient for many steady-state or slow-varying optical signal detection scenarios, such as thermal imaging and environmental monitoring.

The key indicator of the sensitivity of the detector, D^*, depends on the noise level of the device. Figure 4(b) and Fig. S13 in the ESM show the noise current spectra of devices based on four materials at a frequency of 1 Hz, from which the noise equivalent power (NEP) is calculated. Figure 4(c) summarises the responsivity and detectivity of $NbTe_2$ at 4 μm wavelength for different incident optical powers. It can be seen that the responsivity reaches 2.76 mA/W in self-powered mode, and the detection rate reaches up to ~ 10^8 Jones order of magnitude (1.64×10^8 Jones). Notably, the device's responsiveness and detection rate remain stable at different power levels, demonstrating reliable performance.

As shown in Figs. 4(d) and 4(e) and Fig. S15 in the ESM, in both the 4 and 8.47 μm bands, $NbTe_2$, $TaTe_2$, $NbTe_4$, and $TaTe_4$ all exhibit considerable responsivity and detectivity (all in the order of 10^7–10^8 Jones), which fully demonstrates that this class of materials generally possesses effective photoelectric conversion capabilities in the broad-spectrum mid- and long-wave infrared region. Among them, the 2D materials $NbTe_2$ and $TaTe_2$ have relatively better performances. For example, at 4 μm, the response rate of $TaTe_2$ also reaches 2.47 mA/W.

To further assess the stability of the device, we stored it in an air environment at room temperature for an extended period. After 60 days, the photoresponse characteristics remained highly consistent, with the self-driven photocurrent decreasing only slightly to 96.7% of its initial value (Fig. 4(d)). Finally, the photoresponse under incoherent blackbody radiation was characterized to evaluate the detection limit for passive imaging applications (Fig. S17 and Note S1 in the ESM). This result highlights the exceptional environmental stability and long service life of $NbTe_2$-based photodetectors, demonstrating outstanding environmental stability and providing key assurance for practical device implementation. Despite the intrinsic limitation of the response speed of detectors based on the PTE mechanism, the Nb/Ta-Te series of detectors reported in this work exhibits universal, stable and comparable detection performance (D^* ~ 10^8 Jones) and excellent long-term stability in the mid- and long-wavelength infrared bands from 4 to 8.47 μm in the room-temperature, self-powered operating mode. These performance indexes indicate that this class of CDW materials, as a novel mid- and long-wavelength infrared sensitive material system, has a unique application value in the field of low-power infrared sensing without refrigeration and external bias. The significance lies in expanding the diversity of infrared photovoltaic materials and providing a promising material platform for the development of low-cost and easy-to-integrate infrared detection solutions in specific application scenarios.

2.5 AI-driven super-resolution reconstruction for single-pixel photodetector imaging

Image super-resolution reconstruction is a powerful technique for recovering high-resolution images from low-resolution inputs, which is particularly valuable for single-pixel imaging systems [47]. Such systems, while compact and versatile, often suffer from

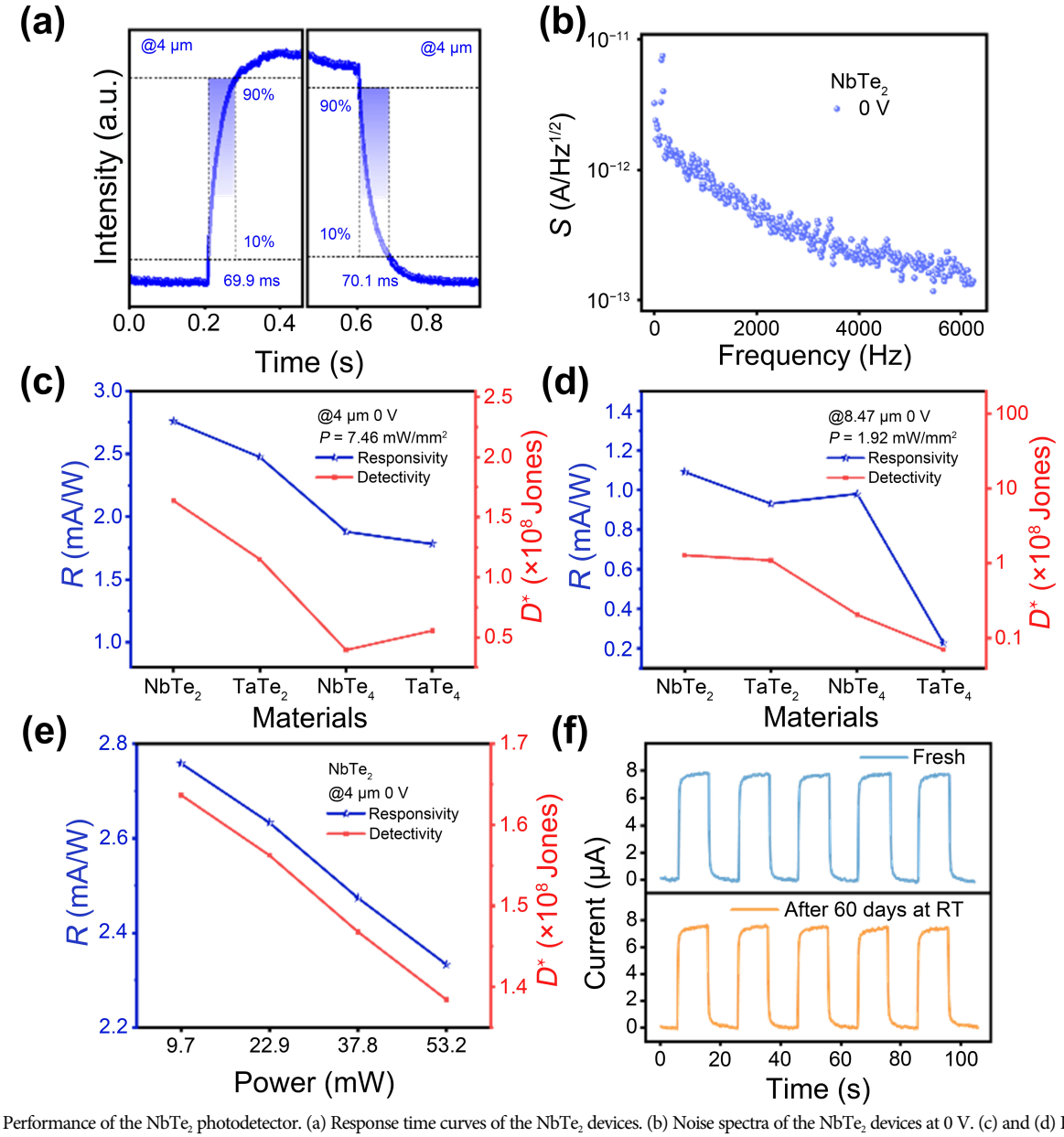

Figure 4 Performance of the $NbTe_2$ photodetector. (a) Response time curves of the $NbTe_2$ devices. (b) Noise spectra of the $NbTe_2$ devices at 0 V. (c) and (d) Responsivity versus detectivity of the four devices in the 4 and 8.47 μm bands at a fixed power density. (e) Variation of responsivity and detectivity with incident optical power at 4 μm for $NbTe_2$. (f) Performance comparison of the $NbTe_2$ devices before and after 60 days in air, showing excellent environmental stability.

environmental disturbances—including noise, temperature fluctuations, and operator-induced variability—that compromise image clarity. Deep learning-based super-resolution reconstruction effectively addresses these limitations by leveraging spatial feature extraction and nonlinear mapping.

As shown in Fig. 5(a), a single-pixel imaging system was constructed using an Nb/Ta-Te self-powered detector. By controlling a 2D translation stage to perform point-by-point scanning of the target mask and recording the photocurrent response of the detector under zero bias, we successfully reconstructed a "DHU" image corresponding to the mask pattern. The reconstructed image was then uploaded to a computer, further processed via a deep neural network for super-resolution reconstruction, and finally distributed to end-users. During measuring (Fig. 5(b)), images were fed into the network, which employed 3 × 3 convolutional kernels and 2 × 2 pooling layers within its encoder-decoder architecture. Thanks to the high clarity of the material-derived photographs, features in the images could be successfully identified after processing through the encoder and decoder sequences. During training, the model achieved a high accuracy of 96.4% and a low loss value of 0.035. As a result, the U-Net model is capable of annotating image features, and the generated images are clearly presented. Figure 5(c) demonstrates the comparison of images before and after neural network processing, where it is clearly observed that the details and clarity of the four types of images—the letters "DHU", a flower, a bird, and leave—are significantly enhanced after super-resolution reconstruction.

This technical solution skillfully integrates the hardware advantages of the Nb/Ta-Te detector, such as room-temperature operation, self-powering capability, and broad-spectrum response, with the software advantages of the U-Net deep learning framework in image enhancement. It enables fast and non-destructive

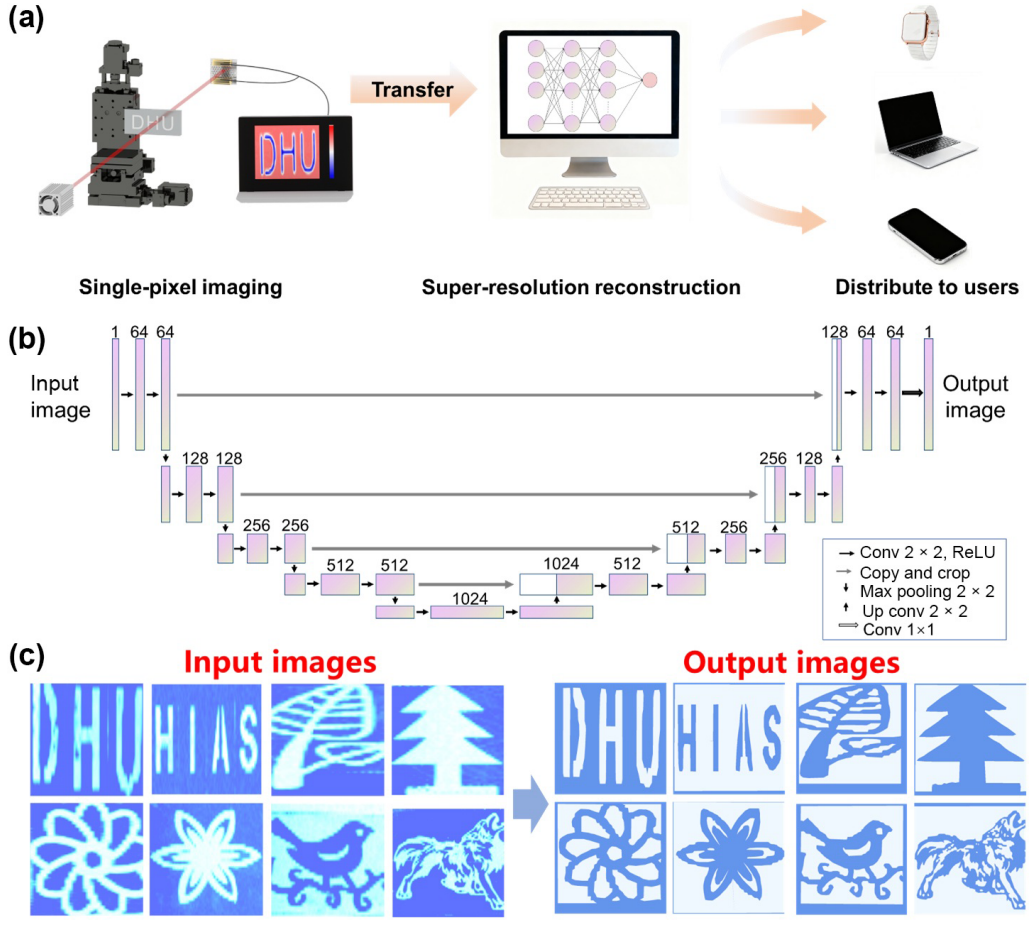

Figure 5 Super-resolution reconstruction of single-pixel infrared imaging. (a) Schematic diagram of the technical workflow for image super-resolution reconstruction. (b) Architecture of the deep learning network based on a U-Net model, which is employed for the image enhancement task. (c) A comparative visualization of the imaging results before (left) and after (right) the super-resolution reconstruction, demonstrating a significant improvement in image clarity and detail.

identification for infrared imaging, providing a feasible technical pathway for developing next-generation lightweight, low-power, and intelligent mid- to long-wave infrared imaging systems. It is worth noting that the image acquisition rate in our current single-pixel imaging demonstration is primarily limited by the mechanical latency of the 2D translation stage rather than the electrical response speed of the photodetector. While the device exhibits a response time of ~ 70 ms (Fig. 4(a)), the physical movement and stabilization of the mechanical stage for each pixel typically require hundreds of milliseconds. To ensure a high signal-to-noise ratio (SNR) and superior image quality during this proof-of-concept phase, an integration time of approximately 0.5–1.0 s was set for each pixel. This duration is well beyond the device's rise time, ensuring that the photocurrent reaches a steady state during data acquisition. Therefore, for the current mechanical scanning system, the device's response speed provides a comfortable margin and does not constitute a limiting factor.

The integration of intelligent transportation and artificial intelligence imposes higher demands on the environmental perception capabilities of autonomous driving, particularly under challenging conditions such as nighttime or adverse weather where visible-light sensors underperform [48]. Building upon our previous research, we propose an intelligent perception scheme based on self-powered mid-/long-wave infrared detectors (Fig. 6). This approach utilizes U-Net for super-resolution reconstruction of images and employs convolutional neural networks to interpret scene information, enabling the vehicle system to generate appropriate driving strategies. Figures 6(a)–6(c) respectively illustrate typical road conditions, feature extraction, and data transmission processes, while Fig. 6(d) presents corresponding system decisions (passing, stopping, cautious driving), validating the potential of this technology for reliable perception and intelligent decision-making in complex environments.

In addition, to assess the applicability of the photodetector in infrared optical communication, we developed an infrared communication system based on the $NbTe_2$ photodetector (Fig. S16(a) in the ESM). The system utilized a 1550 nm laser light source combined with a time-controlled shutter to generate binary optical signals. These signals were converted into electrical signals by the photodetector, enabling efficient transmission of the photoelectric signal. In our experiments, we successfully transmitted a binary infrared light signal encoding the international Morse code distress signal "SOS". Specifically, the laser and the timed shutter generated light pulses corresponding to the "SOS" sequence (Fig. S16(b) in the ESM). The electrical signal received by the detector was processed and accurately decoded into text using the ASCII code, achieving real-time translation from optical signal to text. These results demonstrate that the $NbTe_2$-based photodetector not only possesses ultra-wide spectral detection capabilities but also excels in infrared imaging and communication. Its high sensitivity and accurate decoding capabilities for binary optical signals provide crucial technical support for advanced infrared optical communication technologies.

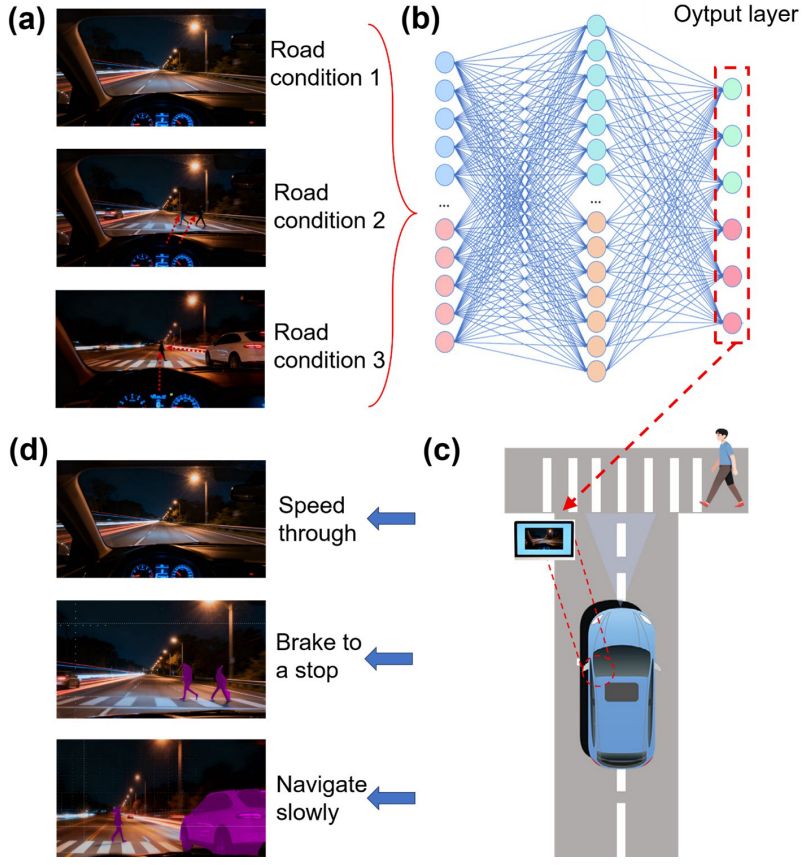

Figure 6 Intelligent infrared perception scheme for autonomous driving. (a) Typical road conditions (clear road, pedestrian-dense scenario, and congested traffic). (b) Super-resolution reconstruction of images via a deep learning network. (c) Transmission of the processed information to the on-board computer. (d) Final driving decisions generated by the system (speed through, brake to stop, and navigate slowly).

3 Conclusions

In summary, we have systematically explored the potential of structurally diverse binary Nb/Ta–Te CDW compounds—namely 1D $NbTe_4$ and $TaTe_4$, and 2D $NbTe_2$ and $TaTe_2$—for mid- and long-wavelength infrared optoelectronic detection. High-quality, structurally well-defined single crystals were successfully synthesized via the chemical vapor transport method. Comprehensive optoelectronic characterization reveals that all four compounds exhibit pronounced mid- and long-wavelength infrared photoresponse dominated by the PTE effect, operating effectively at room temperature and under zero bias (self-powered mode). Spatially resolved photocurrent mapping, confirmed by position-dependent *I*–*V* and *I*–*t* measurements, further demonstrates their uniform response. The fabricated photodetectors show reliable performance at 4 and 8.47 μm, with detectivities (D^*) on the order of 10^7–10^8 Jones, and exhibit excellent long-term environmental stability, underscoring their suitability for room-temperature infrared detection.

Furthermore, single-pixel mid- and long-wavelength infrared imaging was successfully demonstrated using these detectors, and deep-learning-assisted image reconstruction achieved significant image enhancement. This establishes an initial technological framework integrating new materials, core devices, and intelligent sensing, highlighting the feasibility of practical applications. Overall, this work not only broadens the material landscape for mid- and long-wavelength infrared photodetection and reveals the universality of the PTE effect in Nb/Ta–Te CDW compounds, but also provides a competitive materials platform and a viable technological pathway toward next-generation, room-temperature, low-power, and intelligent infrared optoelectronic systems. Future studies may focus on tuning material dimensionality and anisotropy, optimizing device architecture to enhance response speed, and advancing their integration into practical application scenarios.

4 Experimental section

4.1 Starting materials

The following chemicals were purchased and used without further purification: niobium powders (Nb, Macklin, 99.99%), tantalum powders (Ta, Adamas, 99.9%), tellurium ingots (Te, Macklin, Adamas, 99.99%), and iodine flakes (I_2, Alfa Aesar, 99.9%).

4.2 Synthesis of MTe_2 (M = Nb, Ta) single crystals

Single crystals of $NbTe_2$ and $TaTe_2$ were grown using the chemical vapor transport (CVT) method [42]. Nb/Ta powders and Te powders were mixed in a 1:2 molar ratio and placed into a quartz tube (12.5 mm o.d. × 10.5 mm i.d., 20 cm length). A transport agent, 15 mg of I_2, was added to the tube. The quartz tube was then sealed under vacuum (< 10^{-3} mbar) and transferred to a two-zone furnace. The tube was heated for 7 days, with the source zone maintained at 1125 K and the crystallization zone at 1025 K. After heating, the tube was allowed to cool naturally to room temperature. Plate-like single crystals, each exceeding a length of 4 mm, were successfully obtained.

4.3 Synthesis of MTe_4 (M = Nb, Ta) single crystals.

Single crystals of $NbTe_4$ and $TaTe_4$ were grown by the chemical vapor transport (CVT) method [42, 49]. Nb/Ta powders and Te powders were mixed in a 1:4 molar ratio and placed into a quartz tube (12.5 mm o.d. × 10.5 mm i.d., 20 cm length). A transport agent, 15 mg of I_2 was added to the tube. The quartz tube was then sealed under vacuum (< 10^{-3} mbar) and transferred to a two-zone furnace. The tube was heated for 7 days, with the source zone maintained at 1273 K and the crystallization zone at 1073 K. After heating, the tube was allowed to cool naturally to room temperature, yielding barred single crystals.

4.4 Structural characterization

PXRD patterns were collected using a diffractometer (D/max-2500) with Cu Kα radiation at operating conditions of 40 kV and 0.03 A. The microstructure and EDS images of $NbTe_2$, $NbTe_4$, $TaTe_2$, and $TaTe_4$ single crystals were analyzed using a field emission scanning electron microscope (FE-SEM-EDS, JSM-7500F, JEOL, Japan).

4.5 Device fabrication

Two gold electrodes were deposited at each end of the crystal using mask technology to ensure good ohmic contact. These electrodes were subsequently connected to conductive wires using silver paint. A silicon substrate with a 250 nm thick silicon dioxide oxide layer was used to support the sample. Gold electrodes were sputtered onto the single crystal surface using an ion sputter (LEBO Science IS150) at a sputtering voltage of 1.8 kV for 60 s. It is worth noting that while the devices in this work were fabricated using macroscopic bulk single crystals, the terms "1D" and "2D" employed throughout the text refer to the intrinsic crystallographic dimensionality (quasi-1D atomic chains for $NbTe_4$/$TaTe_4$ and quasi-2D atomic layers for $NbTe_2$/$TaTe_2$). This low-dimensional structural nature is the fundamental origin of the observed anisotropic electronic and optoelectronic properties. Figure S9 in the ESM shows the optical photograph and schematic diagram of the device.

4.6 Optoelectronic measurements

The current–voltage characteristics of $NbTe_2$, $TaTe_2$, $NbTe_4$, and $TaTe_4$ photodetectors were measured at room temperature using a Keithley 4200-A SCS source-measure system (Tektronix). To evaluate the mid-wave and long-wave infrared performance of these devices, two quantum cascade lasers with wavelengths of 4 and 8.47 μm were employed as light sources. The response speed of the photodetectors was evaluated using a digital oscilloscope (DS 1102Z-E, Rigol Technologies). The noise spectral density at 0 V was measured using a noise analyzer (SR770 FFT Analyzer) equipped with a preamplifier (SR560).

Electronic Supplementary Material: Supplementary material (phase diagrams of the Nb-Te and the Ta-Te binary; SEM images and corresponding elemental EDS spectra of $NbTe_2$, $TaTe_2$, $NbTe_4$ and $TaTe_4$ single crystals; the XPS spectrum of $NbTe_2$ single crystal; the Seebeck coefficient of Nb/Ta-Te binary materials; noise current spectral density for $TaTe_2$, $NbTe_4$ and $TaTe_4$; detectivities for $NbTe_2$, $TaTe_2$, $NbTe_4$ and $TaTe_4$; photoresponse performance of $TaTe_2$, $NbTe_4$ and $TaTe_4$; response time for $TaTe_2$, $NbTe_4$ and $TaTe_4$; and schematic diagram of the infrared communication system based on the $NbTe_2$ photodetector) is available in the online version of this article at https://doi.org/10.26599/NR.2026.94908526.

Data availability

All data needed to support the conclusions in the paper are presented in the manuscript and the Electronic Supplementary Material. Additional data related to this paper may be requested from the corresponding author upon request.

Acknowledgements

This work was supported by the AI-Enhanced Research Program of Shanghai Municipal Education Commission (No. SMEC-AI-DHUZ-02), Donghua University 2025 Cultivation Project of Discipline Innovation (No. xkcx-202514), the National Natural Science Foundation of China (Nos. 22101045, 62304061, U2141240, and 62175045), the National Key Research and Development Program of China (Nos. 2023YFA1608701 and 2023YFB2806703), and "Pioneer" and "Leading Goose" R&D Program of Zhejiang (No. 2025C02036).

Declaration of competing interest

All the contributing authors report no conflict of interests in this work.

Author contribution statement

H. G. and S. F. X.: Conceptualization, methodology, investigation, data curation, formal analysis, writing – original draft. Z. Y. Y.: Investigation, validation, formal analysis. F. T. S.: Investigation, validation, formal analysis. C. G.: Investigation, data curation. J. Y. Z.: Investigation, validation. W. C.: Investigation, data curation. Y. L. W.: Investigation, validation. Z. S. G.: Investigation, formal analysis. H. X. L.: Investigation, validation. X. Y. Z.: Investigation, data curation. X. H. Z.: Investigation, validation. Q. R. S.: Investigation, formal analysis. L. L. Y.: Supervision, validation, writing – review & editing. Y. Z. W.: Resources, supervision, validation, writing – review & editing. H. Z.: Conceptualization, project administration, funding acquisition, supervision, writing – review & editing. Y. F. S.: Conceptualization, project administration, funding acquisition, resources, supervision, writing – review & editing. H. J. C.: Conceptualization, project administration, funding acquisition, resources, supervision, writing – review & editing. N. D.: Supervision, funding acquisition, writing – review & editing. All the authors have approved the final manuscript.

Use of AI statement

None.

References

[1] Dang, C. H.; Guan, M. X.; Hussain, S.; Wen, W.; Zhu, Y. M.; Jiao, L. Y.; Meng, S.; Xie, L. M. Phase transition photodetection in charge density wave tantalum disulfide. *Nano Lett.* **2020**, *20*, 6725–6731.

[2] Grüner, G. The dynamics of charge-density waves. *Rev. Mod. Phys.* **1988**, *60*, 1129–1181.

[3] Hwang, J.; Ruan, W.; Chen, Y.; Tang, S.; Crommie, M. F.; Shen, Z. X.; Mo, S. K. Charge density waves in two-dimensional transition metal dichalcogenides. *Rep. Prog. Phys.* **2024**, *87*, 044502.

[4] Jung, H.; Jung, J.; Won, C.; Park, H. R.; Cheong, S. W.; Kim, J.; Cho, G. Y.; Yeom, H. W. Chiral pseudogap metal emerging from a disordered van der waals Mott insulator 1*T*-$TaS_{2-x}Se_x$. *Adv. Mater.* **2025**, *37*, 2500287.

[5] Shi, W. J.; Wieder, B. J.; Meyerheim, H. L.; Sun, Y.; Zhang, Y.; Li, Y. W.; Shen, L.; Qi, Y.; Yang, L.; Jena, J. et al. A charge-density-wave topological semimetal. *Nat. Phys.* **2021**, *17*, 381–387.

[6] Sung, H. Y.; Wang, C. H.; Lee, M. P.; Lin, Y. C.; Lin, Y. F.; Huang, C. W.; Wu, W. W. Titanium self-intercalation in titanium diselenide devices: Insights from *in situ* transmission electron microscopy. *Adv. Mater.* **2025**, *37*, 2418557.

[7] Teng, X. K.; Chen, L. B.; Ye, F.; Rosenberg, E.; Liu, Z. Y.; Yin, J. X.; Jiang, Y. X.; Oh, J. S.; Hasan, M. Z.; Neubauer, K. J. et al. Discovery of charge density wave in a Kagome lattice antiferromagnet. *Nature* **2022**, *609*, 490–495.

[8] Han, X. H.; Chen, H.; Tan, H. X.; Cao, Z. Y.; Huang, Z. H.; Ye, Y. H.; Zhao, Z.; Shen, C. M.; Yang, H. T.; Yan, B. H. et al. Atomic manipulation of the emergent quasi-2D superconductivity and pair density wave in a Kagome metal. *Nat. Nanotechnol.* **2025**, *20*, 1017–1025.

[9] Song, H.-L.; Wang, M.-H.; Na, G.-R.; Cui, Z.-H.; Wang, H. Interplay of charge density waves, superconductivity, and band topology in a kagome boron monolayer decorated by dialkaline earth metals. *Phys. Rev. B*, **2026**, *113*, 134515.

[10] Zhang, T. S.; Yu, Z. Y.; Gu, H.; Xiong, S. F.; Chen, Y.; Gao, Z. S.; Wang, Y. L.; Yang, Y.; Sun, F. T.; Zhou, T. R. et al. Canonical $RETe_3$ (*RE* = Rare-earth elements) with charge density wave for room temperature self-powered photodetectors spanning mid-wave infrared band. *Adv. Funct. Mater.* **2025**, *35*, 2501917.

[11] Borisenko, S. V.; Kordyuk, A. A.; Yaresko, A. N.; Zabolotnyy, V. B.; Inosov, D. S.; Schuster, R.; Büchner, B.; Weber, R.; Follath, R.; Patthey, L. et al. Pseudogap and charge density waves in two dimensions. *Phys. Rev. Lett.* **2008**, *100*, 196402.

[12] Sun, X.; Xiao, K. N.; Wei, Y. D.; Mo, W. Q.; Zhang, L. B.; Tian, S. J.; Pan, X. K.; Yang, Y. G.; Lan, S. Q.; Zhang, Y. C. et al. Reconfigurable terahertz optoelectronic logic through charge-density-wave phase engineering. *Nat. Commun.* **2025**, *16*, 4736.

[13] Li, J.; Bai, H.; Li, Y.; Mi, J.; Chen, Q.; Tang, W.; Zhu, H.; Fan, X.; Lu, Y.; Xu, Z. et al. The influence of dimensionality on the charge-density-wave transition and its application on mid-infrared photodetection (Advanced Optical Materials 15/2023). *Adv. Opt. Mater.* **2023**, *11*, 2370054.

[14] Brown, J. O.; Guo, T. S.; Pasqualetti, F.; Balandin, A. A. Charge-density-wave quantum oscillator networks for solving combinatorial optimization problems. *Phys. Rev. Appl.* **2025**, *24*, 024040.

[15] Sheng, S. X.; Abdo, M.; Rolf-Pissarczyk, S.; Lichtenberg, K.; Baumann, S.; Burgess, J. A. J.; Malavolti, L.; Loth, S. Terahertz spectroscopy of collective charge density wave dynamics at the atomic scale. *Nat. Phys.* **2024**, *20*, 1603–1608.

[16] Yang, Y. J.; Xia, M. J.; Zhao, Q. X.; Pan, Z. D.; Dong, H. F.; Zhang, X.; Wu, F. G.; Yang, J. H.; Huo, N. J. Metal-semiconductor phase transition in multilayer VSe_2 for broadband photodetector with high sensitivity. *Adv. Electron. Mater.* **2025**, *11*, 2400682.

[17] Bai, Y. S.; Jian, T.; Pan, Z. M.; Deng, J. H.; Lin, X. Y.; Zhu, C.; Huo, D.; Cheng, Z. B.; Liu, Y.; Cui, P. et al. Realization of multiple charge-density waves in $NbTe_2$ at the monolayer limit. *Nano Lett.* **2023**, *23*, 2107–2113.

[18] Xu, R. Z.; Du, X.; Zhou, J. S.; Gu, X.; Zhang, Q. Q.; Li, Y. D.; Zhao, W. X.; Zheng, F. W.; Arita, M.; Shimada, K. et al. Orbital-selective charge-density wave in $TaTe_4$. *npj Quantum Mater.* **2023**, *8*, 44.

[19] Galvis, J. A.; Fang, A.; Jiménez-Guerrero, D.; Rojas-Castillo, J.; Casas, J.; Herrera, O.; Garcia-Castro, A. C.; Bousquet, E.; Fisher, I. R.; Kapitulnik, A. et al. Nanoscale phase-slip domain walls in the charge density wave state of the Weyl semimetal candidate $NbTe_4$. *Phys. Rev. B* **2023**, *107*, 045120.

[20] Hoque, A. M.; Khokhriakov, D.; Karpiak, B.; Dash, S. P. Charge-spin conversion in layered semimetal $TaTe_2$ and spin injection in van der Waals heterostructures. *Phys. Rev. Res.* **2020**, *2*, 033204.

[21] Zhang, X.; Gu, Q. Q.; Sun, H. G.; Luo, T. C.; Liu, Y. Z.; Chen, Y. Y.; Shao, Z. B.; Zhang, Z. Y.; Li, S. J.; Sun, Y. W. et al. Eightfold fermionic excitation in a charge density wave compound. *Phys. Rev. B* **2020**, *102*, 035125.

[22] de Lima, B. S.; Chaia, N.; Grant, T. W.; de Faria, L. R.; Canova, J. C.; de Oliveira, F. S.; Abud, F.; Machado, A. J. S. Large enhancement of the CDW resistivity anomaly and traces of superconductivity in imperfect samples of $NbTe_4$. *Mater. Chem. Phys.* **2019**, *226*, 95–99.

[23] Yuan, Y. F.; Wang, W. K.; Zhou, Y. H.; Chen, X. L.; Gu, C. C.; An, C.; Zhou, Y.; Zhang, B. W.; Chen, C. H.; Zhang, R. R. et al. Pressure-induced superconductivity in topological semimetal candidate $TaTe_4$. *Adv. Electron. Mater.* **2020**, *6*, 1901260.

[24] Yang, X. J.; Zhou, Y. H.; Wang, M. M.; Bai, H.; Chen, X. L.; An, C.; Zhou, Y.; Chen, Q.; Li, Y. P.; Wang, Z. et al. Pressure induced superconductivity bordering a charge-density-wave state in $NbTe_4$ with strong spin-orbit coupling. *Sci. Rep.* **2018**, *8*, 6298.

[25] Guo, J.; Huang, C.; Luo, H. X.; Yang, H. X.; Wei, L. L.; Cai, S.; Zhou, Y. Z.; Zhao, H. C.; Li, X. D.; Li, Y. C. et al. Observation of three superconducting transitions in the pressurized CDW-bearing compound $TaTe_2$. *Phys. Rev. Mater.* **2022**, *6*, L051801.

[26] Zhang, K.; Zou, N. L.; Ren, Y. R.; Wu, J. Z.; Si, C.; Duan, W. H. Realization of coexisting charge density wave and quantum spin/anomalous hall state in monolayer $NbTe_2$. *Adv. Funct. Mater.* **2022**, *32*, 2111675.

[27] Kar, I.; Dolui, K.; Harnagea, L.; Kushnirenko, Y.; Shipunov, G.; Plumb, N. C.; Shi, M.; Büchner, B.; Thirupathaiah, S. Experimental evidence of a stable 2*H* phase on the surface of layered 1*T*′-$TaTe_2$. *J. Phys. Chem. C* **2021**, *125*, 1150–1156.

[28] Luo, H. H.; Wu, F. F.; He, C. W.; Shen, W. F.; Hu, C. G.; Zhao, W. N.; Yu, P.; Yang, G. W. Intrinsically anisotropic 1D $NbTe_4$ for self-powered polarization-sensitive photodetection. *NPG Asia Mater.* **2024**, *16*, 61.

[29] Xia, C.; Yu, T.; Liu, J. Y.; Li, X.; Wang, J. J.; Ma, S. H.; Yang, G. S.; Qiu, H. L.; Hu, Z. G.; Ye, N. et al. Effective self-powered semimetal $TaTe_2$ photodetector with the thermal localization photothermoelectric effect from ultraviolet to mid-infrared range. *Adv. Opt. Mater.* **2024**, *12*, 2400314.

[30] Zhu, H.; Han, H. Charge density wave in low dimensional materials. *J. Phys.: Conf. Ser.* **2022**, *2338*, 012028.

[31] Barborini, M.; Calandra, M.; Mauri, F.; Wirtz, L.; Cudazzo, P. Excitonic-insulator instability and Peierls distortion in one-dimensional semimetals. *Phys. Rev. B* **2022**, *105*, 075122.

[32] Brütting, W.; Nguyen, P. H.; Rieß, W.; Paasch, G. DC-conduction mechanism and Peierls gap in organic and inorganic charge-density-wave conductors. *Phys. Rev. B* **1995**, *51*, 9533–9543.

[33] Chikina, A.; Lund, H.; Bianchi, M.; Curcio, D.; Dalgaard, K. J.; Bremholm, M.; Lei, S. M.; Singha, R.; Schoop, L. M.; Hofmann, P. Charge density wave generated Fermi surfaces in $NdTe_3$. *Phys. Rev. B* **2023**, *107*, L161103.

[34] Hu, Q. X.; Zheng, Y.; Xu, H. X.; Deng, J. Z.; Liang, C. H.; Yang, F. Z.; Wang, Z. J.; Grinenko, V.; Lv, B. Q.; Ding, H. et al. Evidence for saddle point-driven charge density wave on the surface of heavily hole-doped iron arsenide superconductors. *Nat. Commun.* **2025**, *16*, 253.

[35] O'Leary, E.; Wang, L. L.; Kushnirenko, Y.; Schrunk, B.; Eaton, A.; Herrera-Siklody, P.; Bud'ko, S. L.; Canfield, P. C.; Kaminski, A. Band structure and Fermi surface nesting in $LaSb_2$. *Phys. Rev. B* **2024**, *110*, 035145.

[36] Ritz, E. T.; Fernandes, R. M.; Birol, T. Impact of Sb degrees of freedom on the charge density wave phase diagram of the Kagome metal CsV_3Sb_5. *Phys. Rev. B* **2023**, *107*, 205131.

[37] Zheng, F. P.; Feng, J. Electron-phonon coupling and the coexistence of superconductivity and charge-density wave in monolayer $NbSe_2$. *Phys. Rev. B* **2019**, *99*, 161119.

[38] Das, S.; Paudyal, H.; Margine, E. R.; Agterberg, D. F.; Mazin, I. I. Electron-phonon coupling and spin fluctuations in the ising superconductor $NbSe_2$. *npj Comput. Mater.* **2023**, *9*, 66.

[39] Wegner, A.; Zhao, J.; Li, J.; Yang, J.; Anikin, A. A.; Karapetrov, G.; Esfarjani, K.; Louca, D.; Chatterjee, U. Evidence for pseudo-Jahn-Teller distortions in the charge density wave phase of 1*T*-$TiSe_2$. *Phys. Rev. B* **2020**, *101*, 195145.

[40] van Wezel, J.; Nahai-Williamson, P.; Saxena, S. S. Quasi one-dimensional chains and exciton-phonon interactions in $TiSe_2$. *Phys. Status Solidi (B)* **2010**, *247*, 592–594.

[41] Barajas-Aguilar, A. H.; Irwin, J. C.; Garay-Tapia, A. M.; Schwarz, T.; Paraguay Delgado, F.; Brodersen, P. M.; Prinja, R.; Kherani, N.; Jiménez Sandoval, S. J. Crystalline structure, electronic and lattice-dynamics properties of $NbTe_2$. *Sci. Rep.* **2018**, *8*, 16984.

[42] Jia, L. N.; Huo, C. F.; Yan, X. Q.; Wu, J. Y.; Zhang, Y. Z.; Yang, Y. Y.; Xu, W. X.; Cui, Q. N.; Song, D. H.; Jia, B. H. et al. Ultrafast carrier dynamics in 2D $NbTe_2$ films: Implications for photonic and optoelectronic devices. *ACS Appl. Nano Mater.* **2022**, *5*, 17348–17355.

[43] Wang, F.; Zhang, T.; Xie, R. Z.; Wang, Z.; Hu, W. D. How to characterize figures of merit of two-dimensional photodetectors. *Nat. Commun.* **2023**, *14*, 2224.

[44] Cao, F. R.; Liu, L. S.; Li, L. Short-wave infrared photodetector. *Mater. Today* **2023**, *62*, 327–349.

[45] Pecunia, V.; Anthopoulos, T. D.; Armin, A.; Bouthinon, B.; Caironi, M.; Castellanos-Gomez, A.; Chen, Y. S.; Cho, K.; Clegg, C.; Fang, X. S. et al. Guidelines for accurate evaluation of photodetectors based on emerging semiconductor technologies. *Nat. Photonics* **2025**, *19*, 1178–1188.

[46] Lu, X. W.; Sun, L.; Jiang, P.; Bao, X. H. Progress of photodetectors based on the photothermoelectric effect. *Adv. Mater.* **2019**, *31*, 1902044.

[47] Li, K.; Yang, S. H.; Dong, R. T.; Wang, X. Y.; Huang, J. Q. Survey of single image super-resolution reconstruction. *IET Image Process.* **2020**, *14*, 2273–2290.

[48] Zhang, P. Y.; Sun, Y. H.; Sun, J. C.; Wang, S. T.; Wang, R. M.; Zhang, J. Y. Progress in 2D material-based infrared photodetectors for intelligent vision applications. *Adv. Funct. Mater.* **2025**, *35*, 2502072.

[49] Chen, H. X.; Li, Z. L.; Guo, L. W.; Chen, X. L. Anisotropic magneto-transport and magnetic properties of low-temperature phase of $TaTe_2$. *Europhys. Lett.* **2017**, *117*, 27009.